RSC Advances

PAPER

View Article Online
View Journal | View Issue

Cite this: *RSC Adv.*, 2021, **11**, 10451

Judd–Ofelt parameters and X-ray irradiation results of $MNb_2O_6:Eu^{3+}$ (M = Sr, Cd, Ni) phosphors synthesized *via* a molten salt method

Mustafa İlhan, *[a] Mete Kaan Ekmekçi[b] and İlker Çetin Keskin[c]

Trivalent Eu-activated MNb_2O_6 (M = Sr, Cd, Ni) ceramic phosphors were produced using the molten salt route, which involves a low sintering temperature and provides improved homogeneity. The photoluminescence (PL) and radioluminescence (RL) spectra of phosphors exhibited characteristic Eu^{3+} emissions with $^5F_0 \rightarrow {}^7F_j$ transitions, and strong peaks occurred at the $^5D_0 \rightarrow {}^7F_2$ transition. The PL and RL emissions of $SrNb_2O_6:Eu^{3+}$ decreased over 3 mol%, while both emissions for $CdNb_2O_6:Eu^{3+}$ and $NiNb_2O_6:Eu^{3+}$ increased with increasing Eu^{3+} concentration. The spectral properties of phosphors were evaluated by determining Judd–Ofelt intensity parameters (Ω_2, Ω_4) from the PL emission spectrum. The quantum efficiencies (η_{QE}%) of $MNb_2O_6:Eu^{3+}$ (M = Sr, Cd, Ni) phosphors with the highest emission were found as 61.87%, 41.89%, and 11.87% respectively. Bandwidths ($\sigma_e \times \Delta\lambda_{eff}$) and optical gains ($\sigma_e \times \tau$) of $MNb_2O_6:Eu^{3+}$ (M = Sr, Cd, Ni) phosphors with highest emissions were found as follows; 24.182×10^{-28}, 28.674×10^{-28}, 38.647×10^{-28} cm^3 and 20.441×10^{-25}, 13.790×10^{-25}, 3.987×10^{-25} cm^2 s, respectively, corresponding to the $^5D_0 \rightarrow {}^7F_2$ transition.

Received 25th December 2020
Accepted 23rd February 2021

DOI: 10.1039/d0ra10834k

rsc.li/rsc-advances

1. Introduction

The scientific and technological applications of rare earth (RE) elements have seen significant progress in last few decades due to their unique spectroscopic properties in different host lattices, where their superior chemical and thermal stability are along with their outstanding luminescent yield and color purity. Today, trivalent RE ions have a wide range of applications, such as high-performance luminescent devices, magnets, catalysts, and other functional materials.[1–7] When the host lattice is activated by RE^{3+} ions, besides PL, they can cause changes in RL features. In the radioluminescence mechanism, high-energy ionizing radiation (X-rays, alpha particles, and electrons) instantly transforms into thousands of low-energy photons (1–6 eV). The RL feature is of great importance in many fields, such as high-tech industrial applications, homeland security, radiography, biochemical applications, medical devices, biological safety, particle physics, astrophysics, and nuclear material applications.[6,7]

The oxide compounds of columbite niobates can be expressed as MNb_2O_6 (M = Sr, Cd, Ni, Co, Mg, Mn, *etc.*). The symmetry of MNb_2O_6 easily accepts guest ions of a similar ionic size as the metal and Nb ions of the structure. As the MNb_2O_6 structure, the strontium niobate ($SrNb_2O_6$) compound composed of the SrO_6–NbO_6 octahedral[8,9] stands out due to its luminescence,[7–9] photocatalytic,[10,11] and dielectric[12] properties. The high photocatalytic property of $SrNb_2O_6$ is attributed to its increasing absorption by the change of its crystal structure.[10] The molten salt method, one of the methods used in the synthesis of niobates has a favorite feature due to some advantages, which provides a low sintering temperature, short reaction time, good composition, and improved homogeneity.[7,8] The advantage of the molten salt method can be evaluated by comparing it with the solid-state reaction method. Here, $SrNb_2O_6$ was produced by the solid-state reaction method at 1250 °C for 7 h,[9] whereas $SrNb_2O_6$ was fabricated using the molten salt method at 650 °C for 4 h.[7,8]

In this study, the structural, photoluminescence, and X-ray induced characterizations of $SrNb_2O_6:Eu^{3+}$ were carried out by XRD, SEM, PL, and RL analyses. In addition, the previously reported phosphors of $CdNb_2O_6:Eu^{3+}$ (ref. 13) and $NiNb_2O_6:Eu^{3+}$ (ref. 14) were included in the study, and the Judd–Ofelt intensity parameters and radioluminescence results of $MNb_2O_6:Eu^{3+}$ (M = Sr, Cd, Ni) phosphors were reported by comparison with PL and RL analyses. Also, the grain structures of three compounds were examined by SEM analysis.

2 Experimental

In the synthesis of (Sr, Cd, Ni)$Nb_2O_6:xEu^{3+}$ (x% = 0.5, 3, 6 mol%) and undoped ceramic powders by the molten salt method, as starting materials for each synthesis, strontium

[a]*Department of Environmental Engineering, Faculty of Engineering, Marmara University, Kadıköy, 34722, İstanbul, Turkey. E-mail: mustafa.ilhan@marmara.edu.tr*
[b]*Department of Chemistry, Faculty of Arts and Sciences, Marmara University, Kadıköy, 34722, İstanbul, Turkey*
[c]*Department of Electricity and Energy, Soma Vocational School, Manisa Celal Bayar University, Soma, 45500, Manisa, Turkey*

nitrate ($Sr(NO_3)_2$) (Sigma-Aldrich, 99%), cadmium nitrate tetrahydrate ($Cd(NO_3)_2 \cdot 4H_2O$) (Sigma-Aldrich, 98.5%), nickel nitrate hexahydrate ($Ni(NO_3)_2 \cdot 6H_2O$) (Sigma-Aldrich, 99%), pure niobium oxide (Nb_2O_5) (Alpha Aesar, 99.9%), and Eu_2O_3 (Alpha Aesar, 99.9%) powder were used in the calculated stoichiometric amounts. The x value was taken as "mol", which means 2 Eu atoms due to the Eu_2O_3 compound. The syntheses of (Cd,Ni)Nb_2O_6:Eu^{3+} (ref. 13 and [14]) and $SrNb_2O_6$:Nd^{3+}, Dy^{3+} (ref. 7 and [8]) were reported as intermediate solid solutions. However, the $Sr(NO_3)_2$ amount was reduced slightly to prevent secondary phase formation in the synthesis of $SrNb_2O_6$:Nd^{3+}, Dy^{3+},[7,8] similarly, 0.98 and 0.95 mol were used instead of 1 mol $Sr(NO_3)_2$ for the 3 and 6 mol% Eu^{3+} samples, respectively, corresponding to 2 mol of Nb_2O_5. The stoichiometric amounts of the molten salt mixtures were added to the reactant mixtures. For this purpose, the molten salts to be used and their mixing ratios were, respectively, for strontium niobate synthesis, NaCl : KCl, salt : salt molar ratio 6 : 1 and salt : oxide weight ratio 1 : 1, for cadmium niobate synthesis, Li_2SO_4 : Na_2SO_4, salt : salt molar ratio 1 : 1 and salt : oxide weight ratio 1 : 1, for nickel niobate synthesis, Li_2SO_4 : Na_2SO_4, salt : salt molar ratio 1 : 1 and salt : oxide weight ratio 1 : 1. The starting materials for each compound group were mixed to produce the phosphor powders by the molten salt synthesis method and finely ground in an agate mortar to ensure homogeneity. After that, europium oxide (Eu_2O_3) dopant was added. The final powder mixture was thoroughly mixed in an agate mortar for a final time and re-ground to ensure greater homogeneity. Then, mixtures prepared by weighing for each compound were placed and calcined in alumina crucibles at 650 °C for 4 h for strontium niobate, or at 900 °C for 4 h for cadmium niobate and nickel niobate. Phosphor powders obtained as a result of the heat treatment were washed many times with ultrapure water to remove the ionic salts they contained and vacuum filtered several times. The presence of Cl-ions in the filtrate was checked using qualitative reactions.

The powder samples analyses were carried out by XRD (X-ray diffractometer; D2 PHASER, Bruker Corp., Germany) using Cu-K_α (1.54 Å) radiation in between 2θ = 5–70 °C with a scan speed of 2 °C min^{-1}. SEM micrographs of the samples were taken by scanning electron microscopy (SEM; Inspect S50, FEI Corp., USA) after Au coating. Elemental compositions were determined by energy dispersive spectroscopy (EDS; INCAx-Sight 7274 model; 133 eV resolution 5.9 keV, OXFORD Instruments, England) which was attached to the SEM system (JSM-5910LV, JEOL Corp., Japan). EDS was performed at 20 kV SEM acceleration voltage.

PL (photoluminescence) measurements were recorded on an Edinburgh Instruments (UK) FLSP920 model fluorescence spectrometer with xenon lamp (450 W) continuous wavelength lamps for steady-state measurements. Decay times were taken by μF1 and μF2: 5 W or 60 W pulsed xenon microsecond flashlamps producing short microsecond pulses for decay measurements. Decay curves data (B_1, τ_1, B_2, τ_2) were recorded with a time-correlated single-photon counting (TCSPC) system. Radioluminescence (RL) results were obtained using an Horiba Jobin Yvon spectrometer (Japan), which included a liquid nitrogen-cooled CCD detector and an X-ray irradiation source Machlett OEG-50A. The data for the RL were recorded with a detector integration time of 5 s between 200–1000 nm and 2 mm was chosen for the slit widths (input and output). The operating level of the spectrometer was 30 kV and 15 mA (30 Gy min^{-1}) and it was operated in a dark environment and at room temperature.

3. Results and discussions

3.1 Structural analyses

Fig. 1 shows the X-ray diffraction results of undoped $SrNb_2O_6$ and Eu^{3+}-doped $SrNb_2O_6$ samples. The XRD pattern (JCPDS no: 28-1243) of the samples was indexed by orthorhombic columbite symmetry with the space group *Pbcn*60. The $CdNb_2O_6$:Eu^{3+} (ref. 13) and $NiNb_2O_6$:Eu^{3+} (ref. 14) structures also had the same symmetry, and their symmetry continued up to 6 mol%, while secondary phases were found at low amounts. The XRD-SEM results of $SrNb_2O_6$:Eu^{3+} were investigated in this study, the detailed X-ray diffraction results of the $CdNb_2O_6$:Eu^{3+} and $NiNb_2O_6$:Eu^{3+} have been reported in ref. 13 and [14]. The cell parameters of orthorhombic $SrNb_2O_6$ are $a = 5.592$ Å, $b = 7.722$ Å, $c = 10.989$ Å, and $\alpha = \beta = \gamma = 90°$.[7] On the other hand, it has been reported that the orthorhombic columbite symmetry and monoclinic symmetry almost fully overlap with each other.[15,16] Accordingly, XRD reflections of $SrNb_2O_6$ could be indexed with monoclinic symmetry (space group $P2_1/c$) which exactly fitted with the orthorhombic symmetry.[15,16] Based on the monoclinic symmetry, the cell parameters of $SrNb_2O_6$ are $a = 5.594$ Å, $b = 7.722$ Å, $c = 10.986$ Å, and $\alpha = 90.37°$, $\beta = \gamma = 90°$.[17,18]

The $SrNb_2O_6$ structure composed of corner-shared and edge-shared NbO_6 octahedral aligned along the a-axis and c-axis, respectively, as shown in Fig. 2. The Sr^{2+} and Nb^{5+} cations are surrounded by O^{2-} with 8 and 6 CN (coordination number), and their ionic radii (r) are 1.26 Å and 0.64 Å, respectively.[7,9] There is a cationic site with Wyckoff position 4e for the compatibility of the activator ions within the crystal structure.[9] The Eu^{3+} ions

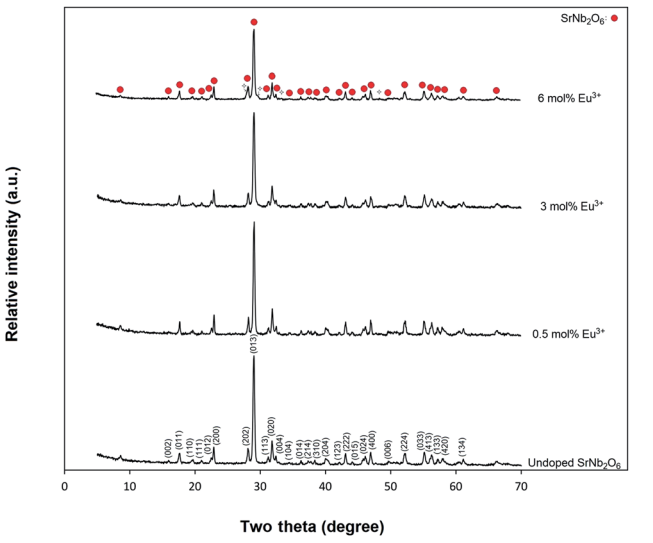

Fig. 1 X-ray diffraction results for undoped $SrNb_2O_6$ and Eu^{3+}-doped $SrNb_2O_6$ powders.

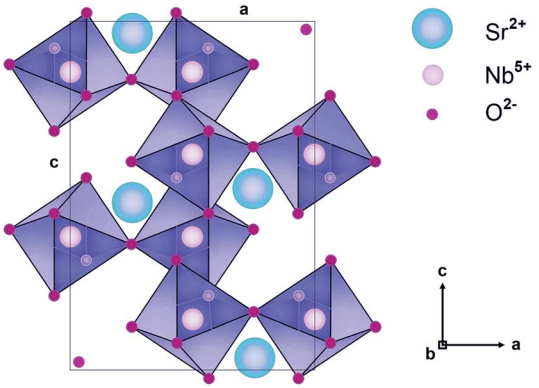

Fig. 2 Schematic illustration of $SrNb_2O_6$ crystal in the direction of the *b* axis.

will occupy the $SrNb_2O_6$ structure with the ionic radii of 0.947 Å for 6 CN and 1.066 Å for 8 CN. On the basis of $SrNb_2O_6$ doping with Eu^{3+}, the Eu^{3+} ions will take place as an intermediate atom, while some Eu^{3+} ions will replace the ions of Sr^{2+}. A small amount of Eu^{3+} ions lead to the formation of a minor amount of $EuNbO_4$ for 6 mol% sample, as seen in the XRD pattern in Fig. 1.

Also, the increase in positive charge due to the inclusion of Eu^{3+} ions will affect the lattice charge balance in the lattice.

SEM micrographs of MNb_2O_6:Eu^{3+} structures (M = Sr, Cd, Ni) for 3 mol% concentration of Eu^{3+} are presented in Fig. 3(a–d). SEM micrographs of Eu^{3+}-doped $SrNb_2O_6$ are given in Fig. 3(a and b) at 2000× and 20 000× magnifications, respectively. The grain morphologies with rod-like shapes exhibited the characteristic structure of $SrNb_2O_6$.[7,8] The thicknesses and lengths of the rods for all the samples varied between 0.06–0.68 and 0.21–12 μm, respectively. The grain shape and size of $CdNb_2O_6$:Eu^{3+} and $NiNb_2O_6Eu^{3+}$ differed in the SEM micrographs given in Fig. 3(c and d) and at 20 000× magnification, respectively. While the grains of Eu^{3+}-doped $CdNb_2O_6$ were irregular, agglomerated, and plate-like shape, the grain sizes varied in the range of 0.5–4 μm. The grain morphologies of Eu^{3+}-doped $NiNb_2O_6$ were round-like shape and relatively less agglomerated, with small grain sizes in the range of 0.1–1 μm. The EDS spectra and elemental compositions (at% and wt%) for 3 mol% Eu^{3+}-doped MNb_2O_6 (M = Sr, Cd, Ni) samples are given in Fig. 4(a–c), respectively. The EDS atomic compositions (%) of the samples are highly compatible with the theoretical atomic values (%).

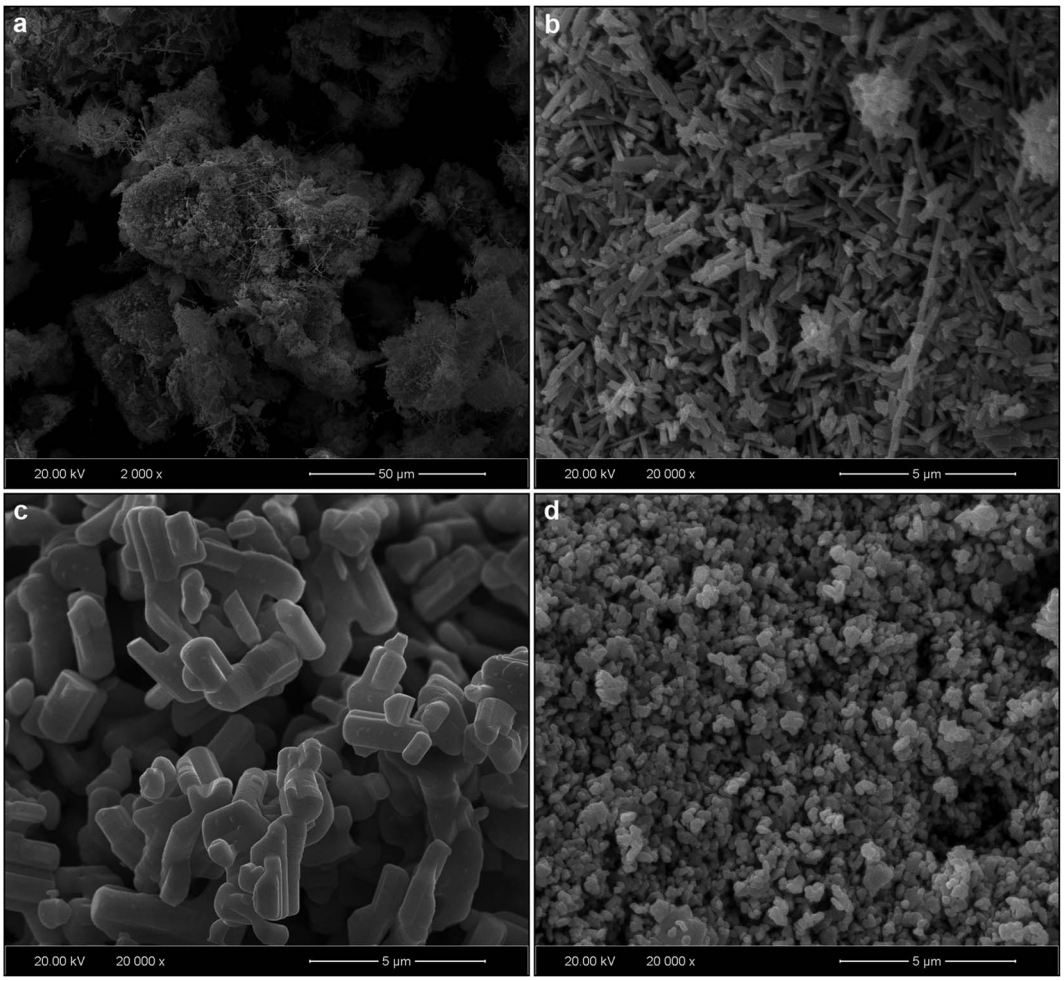

Fig. 3 SEM results of 3 mol% Eu^{3+}-doped MNb_2O_6 samples: (a) SEM micrograph for $SrNb_2O_6$:Eu^{3+} at low (2000×) magnification, and SEM micrographs at high (20 000×) magnification: (b) $SrNb_2O_6$:Eu^{3+}, (c) $CdNb_2O_6$:Eu^{3+}, and (d) $NiNb_2O_6$:Eu^{3+}.

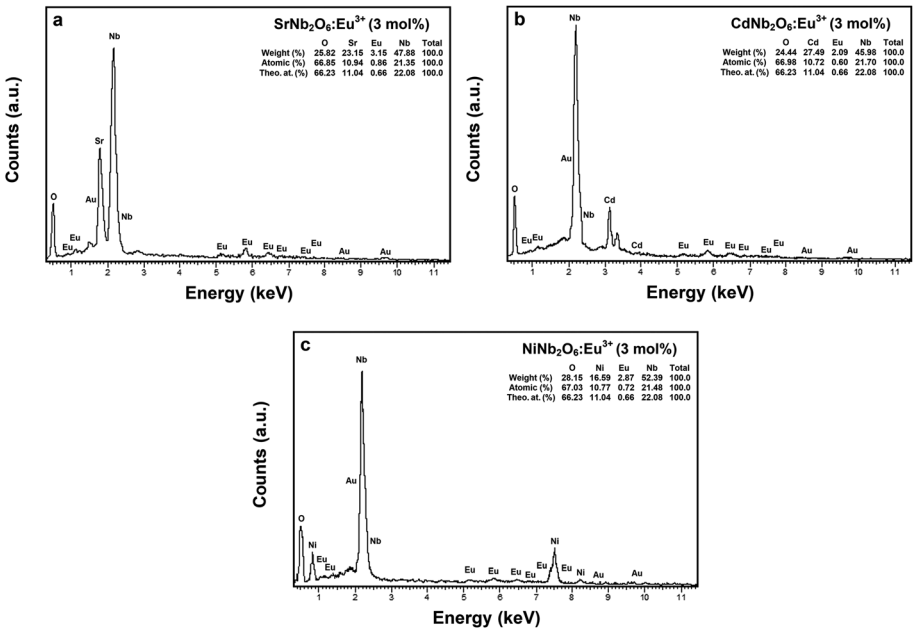

Fig. 4 EDS elemental compositions (wt%, at%) and theoretical atomic values (%) for 3 mol% Eu^{3+}-doped MNb_2O_6 samples: (a) $SrNb_2O_6:Eu^{3+}$, (b) $CdNb_2O_6:Eu^{3+}$, and (c) $NiNb_2O_6:Eu^{3+}$.

3.2 Photoluminescence and radioluminescence analyses

Fig. 5(a–c) show the CT bands and PL excitations of $MNb_2O_6:Eu^{3+}$ (M = Sr, Cd, Ni) phosphors recorded at emission wavelengths of 615.7, 616.2, and 614.0 nm, respectively. PL excitations of the phosphors were assigned to the transitions of $^7F_0 \rightarrow {}^5D_4$, $^7F_0 \rightarrow {}^5G_j$, $^7F_0 \rightarrow {}^5L_6$, $^7F_0 \rightarrow {}^5D_3$, and $^7F_0 \rightarrow {}^5D_2$. The broad CT bands with peak centers at 277.4 nm ($SrNb_2O_6:Eu^{3+}$), 276.6 nm ($CdNb_2O_6:Eu^{3+}$), and 277.7 nm ($NiNb_2O_6:Eu^{3+}$) could be attributed to the Eu^{3+}–O^{2-} charge transfer, which results from the transition of 2p electrons of O^{2-} to the empty 4f orbitals of Eu^{3+} ion.[5,6] Fig. 6(a–c) show the PL emissions of $MNb_2O_6:Eu^{3+}$ (M = Sr, Cd, Ni) phosphors monitored at the $^5D_0$

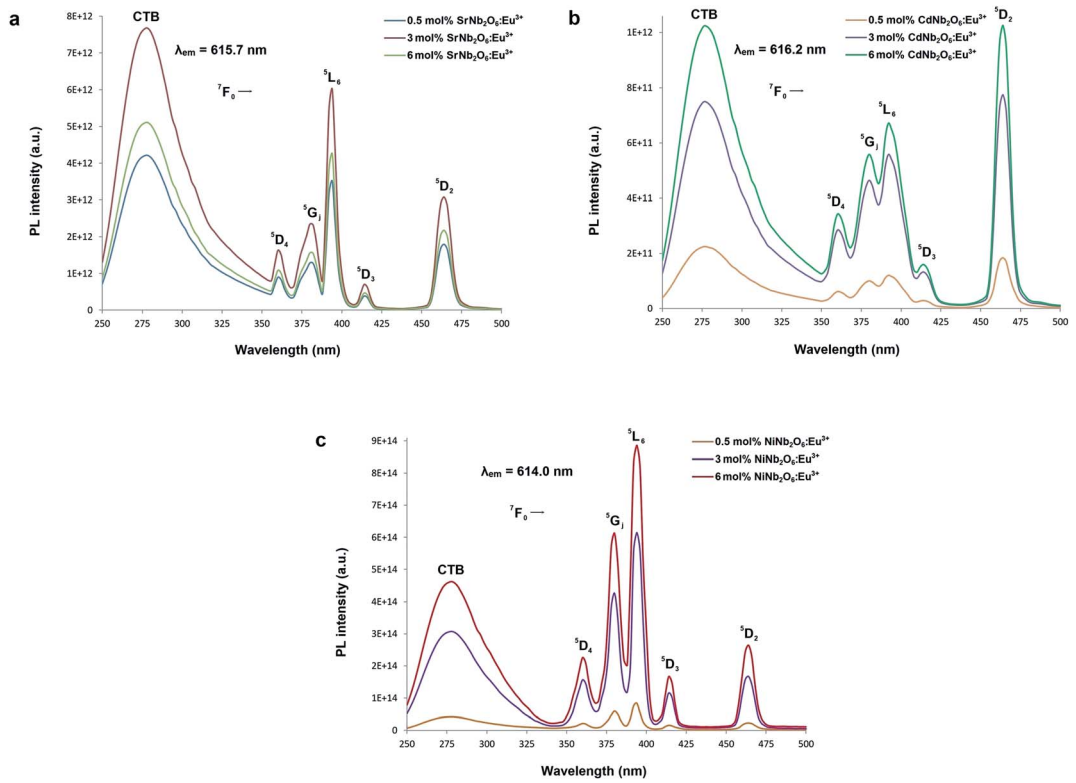

Fig. 5 PL excitation spectra and charge-transfer bands (CTB) of the phosphors: (a) $SrNb_2O_6:Eu^{3+}$, (b) $CdNb_2O_6:Eu^{3+}$, and (c) $NiNb_2O_6:Eu^{3+}$.

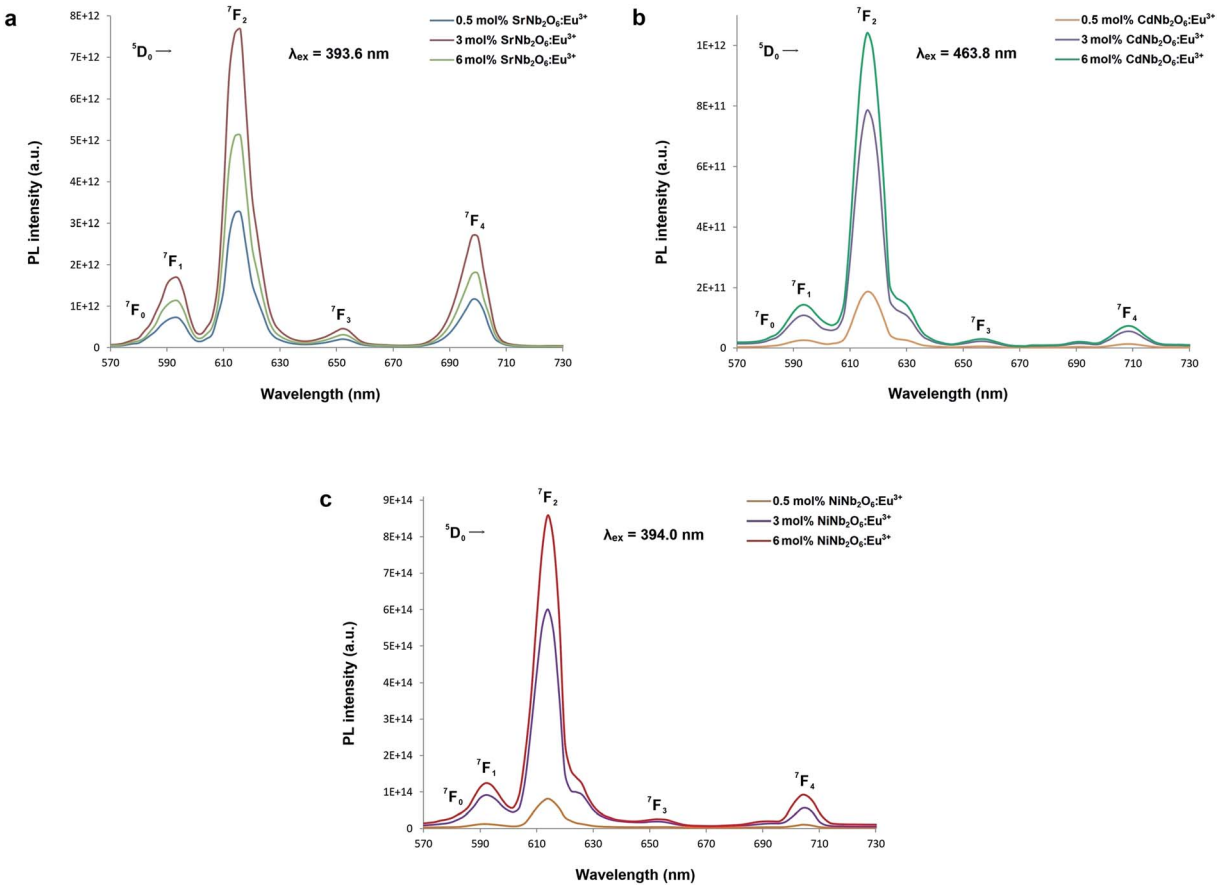

Fig. 6 PL emission spectra of the phosphors: (a) $SrNb_2O_6:Eu^{3+}$, (b) $CdNb_2O_6:Eu^{3+}$, and (c) $NiNb_2O_6:Eu^{3+}$.

$\rightarrow {}^7F_0$, $^5D_0 \rightarrow {}^7F_1$, $^5D_0 \rightarrow {}^7F_2$, $^5D_0 \rightarrow {}^7F_3$, $^5D_0 \rightarrow {}^7F_4$ transitions with the excitation of 393.6, 463.8, and 394.0 nm, respectively. The PL emissions of the $CdNb_2O_6:Eu^{3+}$ and $NiNb_2O_6:Eu^{3+}$ increased up to 6 mol%, while the $SrNb_2O_6:Eu^{3+}$ emission decreased after 3 mol% due to the concentration quenching or nonradiative energy transfer, which originated from the host defects and the distance RE^{3+}–RE^{3+}.[5,6] In all the examples, the emission intensities of the $^5D_0 \rightarrow {}^7F_2$ (electric dipole) transition were higher than the $^5D_0 \rightarrow {}^7F_1$ (magnetic dipole) transition. This indicates that the Eu^{3+} ions occupied crystallographic sites without an inversion center.[19,20]

The radioluminescence (RL) emissions of $MNb_2O_6:Eu^{3+}$ (M = Sr, Cd, Ni) phosphors were monitored with the $^5D_0 \rightarrow {}^7F_0$, $^7F_1$, $^7F_2$, $^7F_3$, $^7F_4$ transitions under X-ray irradiation, as shown in Fig. 7(a–c). Also, the $^5D_0 \rightarrow {}^7F_5$ and $^5D_0 \rightarrow {}^7F_6$ transitions detected with RL are given in the inset figures in Fig. 7(a–c). The RL emissions of the phosphors showed a similarity as in the PL and decreased at 6 mol% of $SrNb_2O_6:Eu^{3+}$. Additionally, in the RL emissions of $SrNb_2O_6:Eu^{3+}$, an extra intensity increase or asymmetry (R) increase occurred at the $^5D_0 \rightarrow {}^7F_2$ transition. Therefore both mechanisms could be compared based on the asymmetry, and the R-value variation of PL–RL emissions depending on the Eu^{3+} concentration is given Fig. 8. The R-values of $MNb_2O_6:Eu^{3+}$ (M = Sr, Cd, Ni) phosphors were found to be 4.38–4.44, 6.58–7.13, 5.68–6.78 for PL, and 6.56–7.15, 6.38–7.42, 6.03–6.89 for RL, respectively. The R-value or ($^5D_0 \rightarrow {}^7F_2$)/($^5D_0 \rightarrow {}^7F_1$) ratio can be used as an indicator to predict the symmetry of the local environment of Eu^{3+} ion; whereby a high R-value indicates an increase in Eu^{3+}–O^{2-} covalency and a low symmetry/more distorted environment.[5] As seen in Fig. 8, the R-values of the PL–RL mechanism for $CdNb_2O_6:Eu^{3+}$ and $NiNb_2O_6:Eu^{3+}$ were close to each other. However, the R-value of RL for $SrNb_2O_6:Eu^{3+}$ was about 50% higher than the R-value of PL. The relatively low asymmetry of $SrNb_2O_6:Eu^{3+}$ in PL increased in RL and reached levels close to other phosphors. Although the same basic transitions occur in PL and RL emissions, they do not contribute equally to the excitation mechanisms. X-ray irradiation of RL does not excite the CTB of the host but instead causes the formation of electron–hole pairs in its conduction and valence bands that recombine at the emission center, in which the energy is ultimately deposited.[7,21] X-ray irradiation can change the dipole moments and emission spectrum of Eu^{3+} in the host. Thus, although the symmetry of the Eu^{3+} local environment decreases to some extent with the high-energy photons of RL, the transformation will likely be temporary and the Eu^{3+} local environment symmetry will return to its initial state when X-ray irradiation is interrupted.[7,21]

The possible PL and RL mechanisms of $MNb_2O_6:Eu^{3+}$ (M = Sr, Cd, Ni) phosphors are schematically illustrated in Fig. 9(a and b), respectively. Fig. 9(a) shows the PL mechanism and indicates the possible pathways in the PL process. Excitation

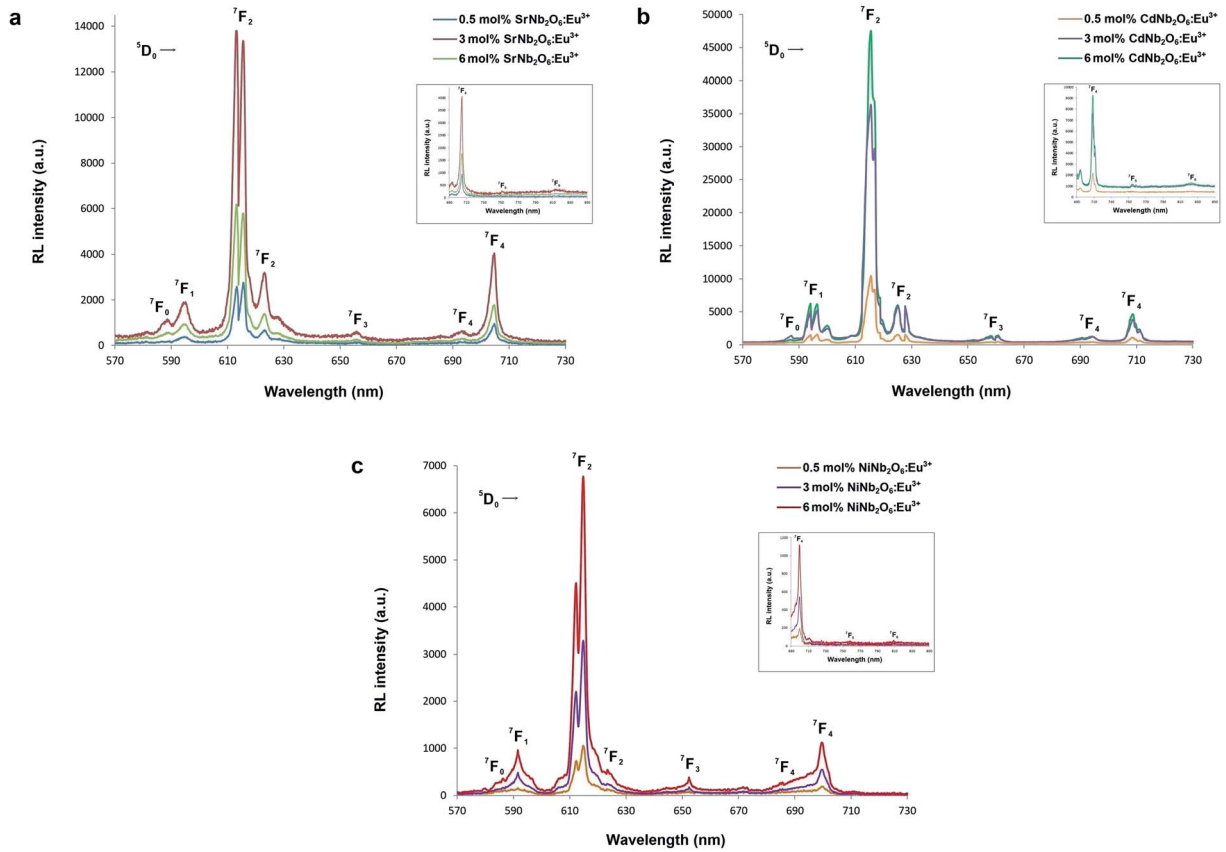

Fig. 7 RL emission spectra of the phosphors: (a) $SrNb_2O_6:Eu^{3+}$, (b) $CdNb_2O_6:Eu^{3+}$, and (c) $NiNb_2O_6:Eu^{3+}$. The $^5D_0 \rightarrow {}^7F_j$ (j = 0, 1, 2, 3, 4) transitions between 570–730 nm, and (inset figures) the $^5D_0 \rightarrow {}^7F_j$ (j = 5, 6) transitions between 690–850 nm.

may consist of two processes, either by transferring the valence band electrons to the charge-transfer band (CTB) or by jumping to the higher levels of Eu^{3+}.[6] Excitation with charge transfer takes place at 276–278 nm while direct excitation of Eu^{3+} occurs at 393.6, 463.8, 394.0 nm. After excitation, the excited electrons come to the lowest excited level ($^5D_0$) of Eu^{3+} by a nonradiative transition. Then it can make ($^5D_0 \rightarrow {}^7F_J$) transitions to the lower levels, in which emissions of Eu^{3+} would occur. The RL possible mechanism of $MNb_2O_6:Eu^{3+}$ (M = Sr, Cd, Ni) phosphors is presented in Fig. 9(b). The electrons of Eu^{3+} in the ground state (^7F_J) promote the conduction band (CB), while the holes stay in the valence band (VB). X-ray induced electrons move in the CB and then part of them transfer to the excitation levels of Eu^{3+}. Also, the formation of traps is possible in the RL mechanism, and a part of the electrons can be captured by the traps, although this is not shown in the figure. Finally, when X-ray-induced electrons move to the ground state, they would be released at the appropriate energy level in which RL emissions take place with the recombination of the electrons and holes.

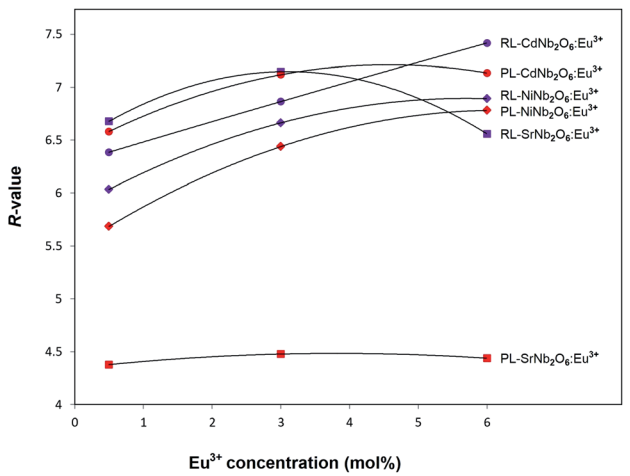

Fig. 8 R-Value variation for PL and RL mechanisms depending on the Eu^{3+} concentration.

3.3. Judd–Ofelt analysis and radiative properties

Judd–Ofelt (JO) intensity parameters are critical to evaluate the performance of luminescent materials.[22,23] Among the RE^{3+} ions, Eu^{3+} has a unique feature for calculation of the JO intensity parameters due to the magnetic dipole transition ($^5D_0 \rightarrow {}^7F_1$) which is independent of the environment and can be used as a reference for transitions arising from the $^5D_0$ level. Using the emission spectra for Eu^{3+}-doped materials, the JO intensity parameters Ω_J (J = 2, 4, 6) can be calculated by eqn (1):[24]

$$\Omega_J = \frac{S_{MD}\left(V_1{}^3\right)}{e^2\left(V_J{}^3\right)} \frac{9n^3}{n(n^2+2)^2} \frac{\int I_1(V_1)}{\left|\langle J\|U^J\|J'\rangle\right|^2 \int I_J(V_J)} \quad (1)$$

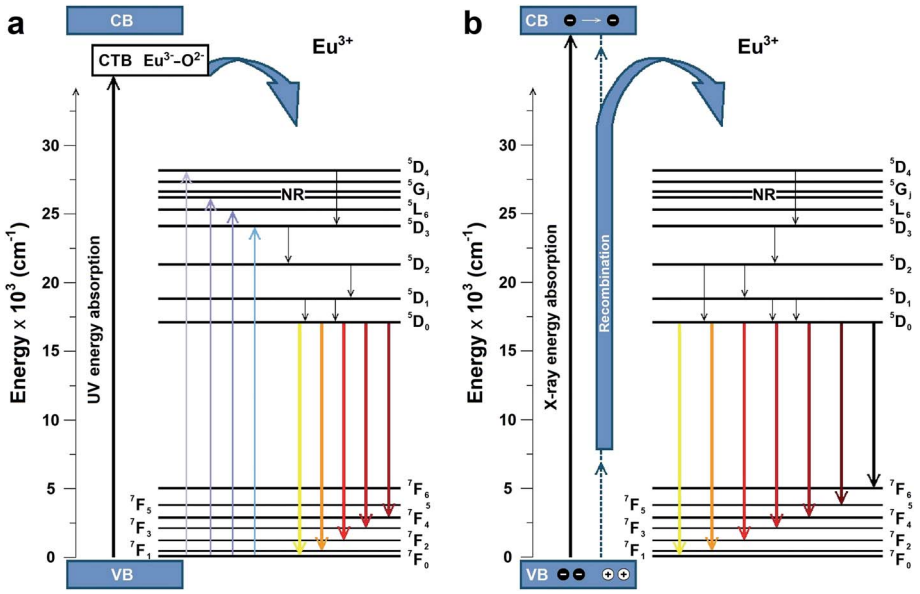

Fig. 9 Schematic energy level diagram to illustrate the possible (a) PL and (b) RL mechanisms.

where V_1, V_J and I_1, I_J are the frequencies and integrated intensities of the $^7F_1$ and ^7F_J ($J = 2, 4, 6$) transitions respectively, $e = 4.803 \times 10^{-10}$ esu (1 esu = $N^{-5/2}$ cm = $gr^{1/2}$ $cm^{3/2}$ s^{-1}) is the elementary charge, n is the refractive index, $S_{MD} = 9.6 \times 10^{-42}$ esu^2 cm^2 is the line strength of the magnetic dipole, which was taken from ref. 24, and $|\langle J\|U^J\|J\rangle|^2$ represent the double-reduced matrix elements of the unit tensor operators, which are independent of the local environment of the ion. All the reduced matrix elements ($|\langle J\|U^J\|J'\rangle|^2$) for electric-dipole (ED) transitions arising from the $^5D_0$ level are zero, except for the levels ^7F_J, (where $J = 2, 4, 6$) $U^2 = 0.0032$, $U^4 = 0.0023$, and $U^6 = 0.0002$.[24] The $^5D_0 \rightarrow {}^7F_J$ ($J = 1, 2, 4, 6$) transitions are used in the calculation of the JO parameters for the radiative transition probability. However, the $^5D_0 \rightarrow {}^7F_J$ ($J = 0, 3, 5$) transitions are forbidden and are not included in the determination of the transition probabilities.[24] According to Judd–Ofelt theory, the spontaneous transition probability (A) is related to its magnetic dipole strength (S_{MD}) and electric-dipole strength (S_{ED}), which can be calculated by eqn (2):[22,23]

$$A(J, J') = \frac{64\pi^4 V^3}{3h(2J+1)}[\chi_{ED} S_{ED} + \chi_{MD} S_{MD}] \quad (2)$$

where J is the total angular momentum of the initial state, and h is Planck's constant. The electric-dipole line strengths (S_{ED}) can be calculated from the JO parameters by eqn (3):[7]

$$S_{ED}(J, J') = e^2 \sum_{J=2,4,6} \Omega_J \left|\langle J\|U^J\|J'\rangle\right|^2 \quad (3)$$

where $|\langle J\|U^J\|J\rangle|^2$ is the symbol of the squared reduced matrix elements, and χ_{ED} and χ_{MD} are the local field corrections for the ED and MD transitions, which can be found by eqn (4) and (5), respectively:

$$\chi_{ED} = \frac{n(n^2+2)^2}{9} \quad (4)$$

$$\chi_{MD} = n^3 \quad (5)$$

where n is the refractive index. The $n = 1.854$ value for $SrNb_2O_6$ was taken from ref. 7. The n value for $CdNb_2O_6$ and $NiNb_2O_6$ can be estimated from the Lorenz–Lorentz formula eqn (6):[25–29]

$$\frac{n^2-1}{n^2+2}\frac{1}{\rho} = \frac{\sum l_i r_i}{M} \quad (6)$$

where M is the molar mass of the compound, l_i is the atomic number of the element in the nominal chemical formula of the compound, ρ is the density, and r_i is the specific refraction of the compound. The refraction index (n) values for $CdNb_2O_6$ and $NiNb_2O_6$ were determined as 1.958 and 2.003, respectively.

The spectral results of the phosphors, JO intensity parameters (Ω_2, Ω_4), radiative transition probabilities ($A(J,J')$), and total radiative transition probabilities ($\sum A(J,J')$ or A_r) are given in Table 1. The Ω_2 parameter shows the short-range effects, while the Ω_4 parameter shows the long-range effects.[25,31] The effects of the Ω_2 parameter are short-range and are associated with the covalence and environmental changes of the Eu^{3+} ion symmetry.[19,20] The high value of Ω_2 or the trend $\Omega_2 > \Omega_4$ is evaluated to show the high covalence of the Eu^{3+}–O^{2-} bond character (ionic or covalent) and the high asymmetry or distortion of the local symmetry of Eu^{3+} sites.[7,31] Accordingly, a high Ω_2 parameter or $\Omega_2 > \Omega_4$ tendency for all the phosphors can be attributed to the low symmetry Eu^{3+} ion and the more covalent or less ionic character of the Eu^{3+}–O^{2-} bond. On the other hand, the effects of the Ω_4 parameter are long-range and are not directly related to the symmetry of the Eu^{3+} ion, but the electron density on the surrounding ligands.[30,31] In all phosphors, the parameter of Ω_4 decreased with increasing Eu^{3+} concentration, which indicated an increase in electron density in the ligands.

The branching ratio (β or β_{cal}) of the Judd–Ofelt theory can be found from the radiative transition probability ($A(J,J')$) and total radiative transition probability $\sum(A(J,J'))$ by eqn (7):[7]

Table 1 J–O parameters (Ω_2, Ω_4), radiative transition and total transition probabilities ($A(J,J')$, (A_r)), branching ratios ((β_{cal}), (β_{exp})), and branching ratio differences (%) of the $MNb_2O_6:Eu^{3+}$ (M = Sr, Cd, Ni) phosphors

Phosphor	Eu^{3+} conc. (mol%)	Eu^{3+} transitions	Ω_2 (10^{-20} cm^2)	Ω_4 (10^{-20} cm^2)	$A(J,J')$ (s^{-1})	A_r (s^{-1})	β_{cal} (%)	β_{exp} (%)	Difference (%)
$SrNb_2O_6:Eu^{3+}$	0.5	$^5D_0 \rightarrow {}^7F_1$	7.148	5.837	92.101	694.935	13.25	14.13	6.20
		$^5D_0 \rightarrow {}^7F_2$			429.055		61.74	63.24	2.37
		$^5D_0 \rightarrow {}^7F_4$			173.779		25.01	22.63	9.49
	3	$^5D_0 \rightarrow {}^7F_1$	7.209	5.818	92.026	697.946	13.19	14.05	6.16
		$^5D_0 \rightarrow {}^7F_2$			432.719		61.99	63.49	2.35
		$^5D_0 \rightarrow {}^7F_4$			173.201		24.82	22.46	9.50
	6	$^5D_0 \rightarrow {}^7F_1$	7.172	5.779	92.194	694.717	13.27	14.15	6.80
		$^5D_0 \rightarrow {}^7F_2$			430.474		61.96	63.44	2.33
		$^5D_0 \rightarrow {}^7F_4$			172.049		24.77	22.41	9.52
$CdNb_2O_6:Eu^{3+}$	0.5	$^5D_0 \rightarrow {}^7F_1$	7.360	1.513	107.954	699.085	15.44	16.09	4.04
		$^5D_0 \rightarrow {}^7F_2$			538.924		77.09	77.40	0.39
		$^5D_0 \rightarrow {}^7F_4$			52.207		7.47	6.51	12.78
	3	$^5D_0 \rightarrow {}^7F_1$	7.788	1.396	107.933	726.332	14.86	15.47	3.95
		$^5D_0 \rightarrow {}^7F_2$			570.238		78.51	78.75	0.31
		$^5D_0 \rightarrow {}^7F_4$			48.161		6.63	5.78	12.86
	6	$^5D_0 \rightarrow {}^7F_1$	7.852	1.388	107.916	730.720	14.77	15.37	3.94
		$^5D_0 \rightarrow {}^7F_2$			574.902		78.67	78.92	0.30
		$^5D_0 \rightarrow {}^7F_4$			47.902		6.56	5.71	12.86
$NiNb_2O_6:Eu^{3+}$	0.5	$^5D_0 \rightarrow {}^7F_1$	8.529	3.235	116.395	926.132	12.57	13.19	4.75
		$^5D_0 \rightarrow {}^7F_2$			685.886		74.06	75.00	1.25
		$^5D_0 \rightarrow {}^7F_4$			123.851		13.37	11.81	11.72
	3	$^5D_0 \rightarrow {}^7F_1$	9.658	2.270	116.375	979.958	11.88	12.40	4.21
		$^5D_0 \rightarrow {}^7F_2$			776.661		79.25	79.82	0.70
		$^5D_0 \rightarrow {}^7F_4$			86.922		8.87	7.79	12.21
	6	$^5D_0 \rightarrow {}^7F_1$	10.023	2.726	116.340	1043.388	11.15	11.66	4.37
		$^5D_0 \rightarrow {}^7F_2$			822.662		78.85	79.54	0.88
		$^5D_0 \rightarrow {}^7F_4$			104.386		10.00	8.80	12.06

$$\beta(\%) = \frac{A(J,J')}{\sum A(J,J')} \times 100\% \quad (7)$$

The branching ratios (β_{cal}) of $^5D_0 \rightarrow {}^7F_2$ transition for $CdNb_2O_6:Eu^{3+}$ and $NiNb_2O_6:Eu^{3+}$ were found as 77.09–78.67% and 74.06–79.25%, respectively. The $SrNb_2O_6:Eu^{3+}$ had a relatively low branching ratio ranging from 61.74–61.99%, for which the results are given in Table 1. The β_{cal} values of the $^5D_0 \rightarrow {}^7F_2$ transition for all phosphors were over 60%. The high value of branching ratio ($\beta > 50$) indicated a potential laser emission.[7,24] The branching ratios (β_{cal}) of the Judd–Ofelt theory can be evaluated using experimental branching ratios (β_{exp}), which can be obtained directly from the emission spectrum. On the other hand, the intrinsic error of the Judd–Ofelt theory in describing spectral intensities is usually about 15%.[7,32] Accordingly, differences between the experimental (β_{exp}) and calculated values (β_{cal}) for all samples occurred between 0.3–12.86%, and they were all below 15% (Table 1).

In the Judd–Ofelt calculation, the Ω_2 and Ω_4 parameters were used, but the Ω_6 parameter was not included since the $^5D_0 \rightarrow {}^7F_6$ transition remaining in the infrared region could not be detected by PL. Similar studies have been reported using the Ω_2 and Ω_4 parameters for JO calculations.[24,30] The $^5D_0 \rightarrow {}^7F_6$ transition outside the visible spectrum is very weak in many materials.[24] In this study, the weak intensity of the $^5D_0 \rightarrow {}^7F_6$ transition detected by RL in Fig. 7(a–c) supports this situation. Based on the $^5D_0 \rightarrow {}^7F_6$ transition observed by RL, the Ω_6 parameters were determined for the samples with the highest emissions intensity. The Ω_6 parameters and total radiative transition probabilities ($\sum A(J,J')$ or A_r) of the $^5D_0 \rightarrow {}^7F_6$ transition were estimated as 2.226×10^{-20}, 1.103×10^{-20}, 0.155×10^{-20} cm^2, and 3.636, 2.116, 0.341 s^{-1} for 3 mol% ($SrNb_2O_6:Eu^{3+}$), 6 mol% ($CdNb_2O_6:Eu^{3+}$), 6 mol% ($NiNb_2O_6:Eu^{3+}$), respectively. The branching ratios (β_{cal}) of the $^5D_0 \rightarrow {}^7F_6$ transition (or the ratio of the $^5D_0 \rightarrow {}^7F_6$ transition probability to the total radiative transition probability) were found in the range of 0.03–0.52%. Also, the branching ratios (β_{exp}) of the $^5D_0 \rightarrow {}^7F_6$ transition from the emission spectra were between 0.18–0.40%. Accordingly, based on the determination of the branching ratios using the RL spectra, the effect of the $^5D_0 \rightarrow {}^7F_6$ transition on the quantum efficiency or other radiative parameters was negligibly minimal, and its exclusion will not have a significant effect.

Fig. 10(a–c) show the decay curves of $MNb_2O_6:Eu^{3+}$ (M = Sr, Cd, Ni) phosphors for $^5D_0 \rightarrow {}^7F_2$ transitions (λ_{em} = 615.7, 616.2, 614.0 nm) recorded with excitations at 393.6, 463.8, and 394.0 nm, respectively. The observed lifetime or average decay (τ) curves can be established by the following two-time temporal dependence in eqn (8):[6]

$$I^L_{(t)} = I^L_{(0)} + B_1 \exp\frac{t_0 - t}{\tau_1} + B_2 \exp\frac{t_0 - t}{\tau_2} \quad (8)$$

where the luminescence intensities are $I^L_{(t)}$ and $I^L_{(0)}$, the fitting constants are B_1 and B_2, and the short and long lifetimes for the

exponential components are τ_1 and τ_2 respectively. The average (observed) lifetime (τ) can be calculated through eqn (9) according to the variables in eqn (8):[6]

$$\tau = \frac{B_1\tau_1^2 + B_2\tau_2^2}{B_1\tau_1 + B_2\tau_2} \quad (9)$$

The observed lifetimes (τ) of the MNb_2O_6:Eu^{3+} (M = Sr, Cd, Ni) phosphors for the $^5D_0$ level varied from 914.36, 673.35, 119.08 to 828.69, 573.29, 113.75 μm, respectively (Table 2). The observed lifetime (τ) represents the sum of nonradiative (τ_{nr}) and the radiative (τ_r) lifetimes, which are expressed by eqn (10). The value of the radiative (experimental) lifetime (τ_r) can be determined from the total radiative transition probability (A_r) by eqn (11):

$$\tau = \tau_r + \tau_{nr} \quad (10)$$

$$\tau_r = \frac{1}{A_r} \quad (11)$$

The radiative lifetime can also be found theoretically by direct calculation from eqn (12), which is related to the emission spectrum of Eu^{3+}.[24,32]

$$\tau_{th} = \frac{{n_1}^3}{14.65}\frac{I_1}{I_{tot}} \quad (12)$$

where τ_{th} is the theoretical radiative lifetime, I_1 is the integrated intensity of the $^5D_0 \rightarrow {}^7F_1$ transition, I_{tot} is the total integrated intensity, and n is the refractive index. The quantum efficiency (η_{QE}) of a phosphor can be defined by the ratio of the number of photons emitted (observed lifetime: τ) to the number of photons absorbed (radiative lifetimes: τ_r). Accordingly, the quantum efficiency (η_{QE}) and theoretical quantum efficiency (η_{QE}^{th}) can be determined by eqn (13) and (14), respectively:

$$\eta_{QE} = \frac{\tau}{\tau_r} \quad (13)$$

$$\eta_{QE}^{th} = \frac{\tau}{\tau_{th}} \quad (14)$$

A comparison of the radiative lifetimes (τ_r, τ_{th}) and quantum efficiencies (η_{QE}, η_{QE}^{th}) of MNb_2O_6:Eu^{3+} (M = Sr, Cd, Ni) phosphors was performed and the results are given in Table 2. The η_{QE}% values for the $SnNb_2O_6$:Eu^{3+} and $CdNb_2O_6$:Eu^{3+} were estimated as follows: 57.57–63.54% and 41.89–47.07%, respectively. However, the η_{QE}% value of $NiNb_2O_6$:Eu^{3+} showed a low efficiency and varied between 11.22–11.88%. The differences of the η_{QE}% (calculated-JO) and η_{QE}^{th} (theoretical) for $SnNb_2O_6$:Eu^{3+} varied between 0.41–0.69%, whereas the compatibility of the efficiencies for $CdNb_2O_6$:Eu^{3+} and $NiNb_2O_6$:Eu^{3+} decreased somewhat and the difference varied between 4.83–5.99 and 2.92–7.16, respectively (Table 2).

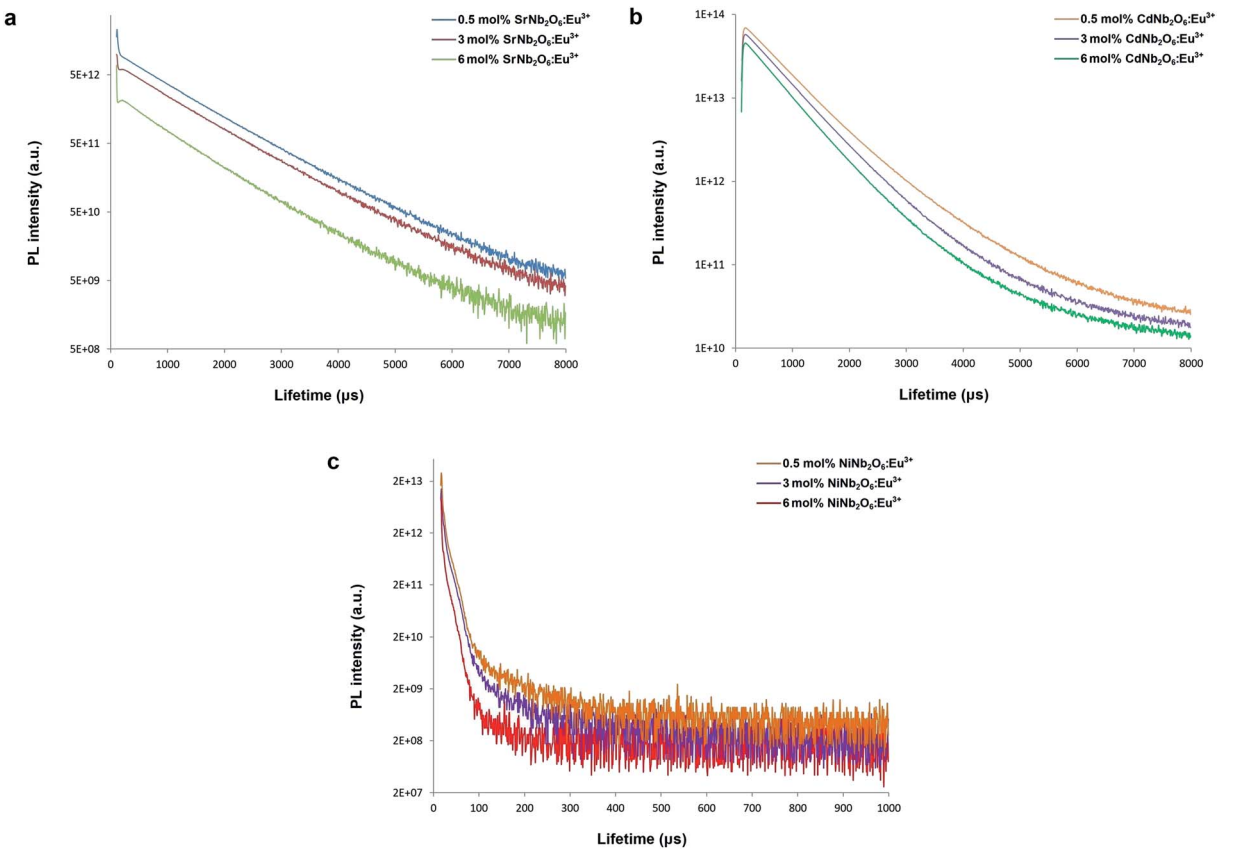

Fig. 10 PL lifetime curves for $^5D_0 \rightarrow {}^7F_2$ transition of the phosphors: (a) $SrNb_2O_6$:Eu^{3+}, (b) $CdNb_2O_6$:Eu^{3+}, and (c) $NiNb_2O_6$:Eu^{3+}.

Table 2 The radiative lifetimes (τ_r), theoretical radiative lifetimes (τ_{th}), observed lifetimes (τ), quantum efficiencies (η_{QE}), theoretical quantum efficiencies (η_{QE}^{th}), and quantum efficiency differences (%) of the $MNb_2O_6:Eu^{3+}$ (M = Sr, Cd, Ni) phosphors

Phosphor	Eu^{3+} conc. (mol%)	τ_r (μs)	τ_{th} (μs)	τ (μs)	η_{QE} (%)	η_{QE}^{th} (%)	Difference (%)
$SrNb_2O_6:Eu^{3+}$	0.5	1438.98	1429.07	914.36	63.54	63.98	0.69
	3	1432.78	1426.16	886.52	61.87	62.16	0.46
	6	1439.43	1433.49	828.69	57.57	57.81	0.41
$CdNb_2O_6:Eu^{3+}$	0.5	1430.44	1344.79	673.35	47.07	50.07	5.99
	3	1376.78	1308.06	609.02	44.24	46.56	4.99
	6	1368.51	1302.47	573.29	41.89	44.02	4.83
$NiNb_2O_6:Eu^{3+}$	0.5	1080.76	1002.41	119.08	11.03	11.88	7.16
	3	1020.45	989.21	115.91	11.36	11.72	3.06
	6	958.42	930.47	113.75	11.87	12.22	2.92

The stimulated emission cross-section (σ_e) is an important factor to predict the laser performance of a material. The stimulated emission cross-section (σ_e) between the states J and J' having a probability of $A(J,J')$ is given by eqn (15):[7,20]

$$\sigma_e(\lambda_p)(J,J') = \left[\frac{(\lambda_p)^4}{8\pi c n^2 \Delta\lambda_{eff}}\right] A(J,J') \quad (15)$$

where c is the velocity of light, λ_p is the emission peak wavelength, $\Delta\lambda_{eff}$ is the effective bandwidth of the emission transition and n is the refractive index of the matrix. The stimulated emission cross-section (σ_e), gain bandwidth ($\sigma_e \times \Delta\lambda_{eff}$), the effective bandwidth of emission transition ($\Delta\lambda_{eff}$), and the optical gain ($\sigma_e \times \tau$) results are given in Table 3. The large σ_e value for the potential laser performance at room temperature is an attractive feature for low threshold and high gain laser applications.[7] The σ_e parameters of the $MNb_2O_6:Eu^{3+}$ (M = Sr, Cd, Ni) phosphors were found as $^7F_2 > {}^7F_4 > {}^7F_1$. The product of the σ_e and $\Delta\lambda_{eff}$ is another important parameter and helps predict the gain bandwidth ($\sigma_e \times \Delta\lambda_{eff}$) of the optical amplifier. The high values of the product are better for the performance of the amplifier.[7] The gain bandwidths ($\sigma_e \times \Delta\lambda_{eff}$) of the $MNb_2O_6:Eu^{3+}$ (M = Sr, Cd, Ni) phosphors with the highest emission were determined as follows: 24.182×10^{-28}, 28.674×10^{-28}, and 38.647×10^{-28} cm^3, respectively, corresponding to $^5D_0 \rightarrow {}^7F_2$ transition. The product of the σ_e and observed lifetime (τ) is an important consideration for high optical amplifier gain.[7,33]

Table 3 The effective bandwidth of the emission transitions ($\Delta\lambda_{eff}$), stimulated emission cross-sections (σ_e), gain bandwidths ($\sigma_e \times \Delta\lambda_{eff}$), and optical gains ($\sigma_e \times \tau$) of the $MNb_2O_6:Eu^{3+}$ (M = Sr, Cd, Ni) phosphors

Phosphor	Eu^{3+} conc. (mol%)	Eu^{3+} transitions	$\Delta\lambda_{eff}$ (nm)	σ_e ($\times 10^{-22}$ cm^2)	$\sigma_e \times \Delta\lambda_{eff}$ ($\times 10^{-28}$ cm^3)	$\sigma_e \times \tau$ ($\times 10^{-25}$ cm^2 s)
$SrNb_2O_6:Eu^{3+}$	0.5	$^5D_0 \rightarrow {}^7F_1$	12.10	3.627	4.388	
		$^5D_0 \rightarrow {}^7F_2$	10.08	23.788	23.977	21.750
		$^5D_0 \rightarrow {}^7F_4$	11.03	14.452	15.933	
	3	$^5D_0 \rightarrow {}^7F_1$	12.15	3.613	4.389	
		$^5D_0 \rightarrow {}^7F_2$	10.49	23.057	24.182	20.441
		$^5D_0 \rightarrow {}^7F_4$	11.21	14.161	15.880	
	6	$^5D_0 \rightarrow {}^7F_1$	12.12	3.618	4.387	
		$^5D_0 \rightarrow {}^7F_2$	10.34	23.269	24.056	19.283
		$^5D_0 \rightarrow {}^7F_4$	11.13	14.168	15.775	
$CdNb_2O_6:Eu^{3+}$	0.5	$^5D_0 \rightarrow {}^7F_1$	14.36	3.233	4.641	
		$^5D_0 \rightarrow {}^7F_2$	11.41	23.552	26.880	15.859
		$^5D_0 \rightarrow {}^7F_4$	12.42	3.683	4.574	
	3	$^5D_0 \rightarrow {}^7F_1$	15.19	3.055	4.642	
		$^5D_0 \rightarrow {}^7F_2$	11.50	24.727	28.442	15.059
		$^5D_0 \rightarrow {}^7F_4$	12.80	3.297	4.219	
	6	$^5D_0 \rightarrow {}^7F_1$	15.85	2.929	4.643	
		$^5D_0 \rightarrow {}^7F_2$	11.92	24.055	28.674	13.790
		$^5D_0 \rightarrow {}^7F_4$	12.91	3.251	4.197	
$NiNb_2O_6:Eu^{3+}$	0.5	$^5D_0 \rightarrow {}^7F_1$	12.96	3.657	4.737	
		$^5D_0 \rightarrow {}^7F_2$	10.91	29.546	32.222	3.518
		$^5D_0 \rightarrow {}^7F_4$	9.11	11.060	10.081	
	3	$^5D_0 \rightarrow {}^7F_1$	13.39	3.537	4.737	
		$^5D_0 \rightarrow {}^7F_2$	10.90	33.487	36.486	3.881
		$^5D_0 \rightarrow {}^7F_4$	9.63	7.345	7.075	
	6	$^5D_0 \rightarrow {}^7F_1$	13.49	3.512	4.738	
		$^5D_0 \rightarrow {}^7F_2$	11.03	35.054	38.647	3.987
		$^5D_0 \rightarrow {}^7F_4$	10.93	7.777	8.497	

The optical gains ($\sigma_e \times \tau$) of $MNb_2O_6:Eu^{3+}$ (M = Sr, Cd, Ni) varied between 19.283–21.750 $\times 10^{-25}$, 13.790–15.859 $\times 10^{-25}$, and 3.518–3.987 $\times 10^{-25}$ cm^2 s, respectively. The large values of the stimulated emission cross-section, gain bandwidth, optical gain, and lifetime support that $MNb_2O_6:Eu^{3+}$ (M = Sr, Cd, Ni) phosphors can be helpful for the improvement of the red lasing and red color applications for display devices.

4. Conclusion

$MNb_2O_6:Eu^{3+}$ (M = Sr, Cd, Ni) crystal powders synthesized by the molten salt method have an orthorhombic/monoclinic symmetry. SEM micrographs of Eu^{3+}-doped $SrNb_2O_6$ exhibited characteristic nanorods for the grain structure, while the grain morphologies of Eu^{3+}-doped $CdNb_2O_6$ and $NiNb_2O_6$ differed in size and shape. The emissions of the phosphors were monitored in PL and RL with the $^5D_0 \rightarrow {}^7F_J$ (J = 0–4) and $^5D_0 \rightarrow {}^7F_J$ (J = 0–6) transitions of Eu^{3+}, respectively. The RL emissions of $SrNb_2O_6:Eu^{3+}$ exhibited an extra increase at the $^5D_0 \rightarrow {}^7F_2$ (electric dipole) transition, which was related to the decrease in local symmetry of Eu^{3+}; however, this same effect was not seen for $CdNb_2O_6:Eu^{3+}$ and $NiNb_2O_6:Eu^{3+}$. By determining the Judd–Ofelt intensity parameters (Ω_2, Ω_4) from the emission spectrum, we calculated the radiative transition probabilities ($A(J,J')$), branching ratios (β_{cal}), and radiative lifetimes (τ_r). The branching ratio difference of the measured (β_{exp}) from the emission spectrum and that calculated (β_{cal}) from the JO parameters for all samples varied by 0.3–12.86%, which were all less than 15%. The high Ω_2 value or $\Omega_2 > \Omega_4$ tendency for all the phosphors indicated the low symmetry Eu^{3+} ion and the more covalent character of the Eu^{3+}–O^{2-} bond. The order of quantum efficiencies (η_{QE}%) was found to be: $SrNb_2O_6:Eu^{3+} > CdNb_2O_6:Eu^{3+} > NiNb_2O_6:Eu^{3+}$. The quantum efficiencies (η_{QE}) of the phosphors deviated slightly from the theoretically calculated quantum efficiencies (η_{QE}^{th}). The bandwidths ($\sigma_e \times \Delta\lambda_{eff}$) and optical gains ($\sigma_e \times \tau$) were found to follow the trend: $SrNb_2O_6:Eu^{3+} < CdNb_2O_6:Eu^{3+} < NiNb_2O_6:Eu^{3+}$ and $SrNb_2O_6:Eu^{3+} > CdNb_2O_6:Eu^{3+} > NiNb_2O_6:Eu^{3+}$, respectively. These results point out that $MNb_2O_6:Eu^{3+}$ (M = Sr, Cd, Ni) phosphors with strong emissions at $^5D_0 \rightarrow {}^7F_2$ transition could be interesting candidates for RE-doped red phosphor applications and for future study.

Conflicts of interest

There are no conflicts to declare.

Acknowledgements

We would like to thank to Marmara University Research Fund (Project No: FEN-A–110718–0393) for the financial support for this study.

References

1 S. Saha, S. Das, U. K. Ghorai, N. Mazumder, B. K. Gupta and K. K. Chattopadhyay, *Dalton Trans.*, 2013, **42**, 12965–12974.
2 C. Yu, B. Chen, X. Zhang, X. Li, J. Zhang, S. Xu, H. Yu, J. Sun, Y. Cao and H. Xia, *Phys. Chem. Chem. Phys.*, 2020, **22**, 7844–7852.
3 Y. Zhang, B. Chen, S. Xu, X. Li, J. Zhang, J. Sun, X. Zhang, H. Xia and R. Hua, *Phys. Chem. Chem. Phys.*, 2018, **20**, 15876–15883.
4 B. Tian, B. Chen, Y. Tian, X. Li, J. Zhang, J. Sun, H. Zhong, L. Cheng, S. Fu, H. Zhong, Y. Wang, X. Zhang, H. Xiac and R. Hua, *J. Mater. Chem. C*, 2013, **1**, 2338–2344.
5 M. İlhan, Synthesis, *Int. J. Appl. Ceram. Technol.*, 2017, **14**, 1134–1143.
6 M. İlhan and İ. Ç. Keskin, *Dalton Trans.*, 2018, **47**, 13939–13948.
7 M. İlhan and İ. Ç. Keskin, *Phys. Chem. Chem. Phys.*, 2020, **22**, 19769–19778.
8 M. K. Ekmekçi, M. İlhan, A. Ege and M. Ayvacıklı, *J. Fluoresc.*, 2017, **27**, 973–979.
9 J. Xue, Y. Guo, B. K. Moon, S. H. Park, J. H. Jeong, J. H. Kim and L. Wang, *Opt. Mater.*, 2017, **66**, 220–229.
10 R. C. Ropp, *Encyclopedia of the Alkaline Earth Compounds*, Elsevier Publications, Oxford, UK, 2013.
11 I. S. Cho, S. Lee, J. H. Noh, D. W. Kim, D. K. Lee, H. S. Jung, D. W. Kim and K. S. Hong, *J. Mater. Chem.*, 2010, **20**, 3979–3983.
12 K. N. Singh and P. K. Bajpai, *World J. Condens. Matter Phys.*, 2011, **1**, 37–48.
13 M. K. Ekmekçi, M. Erdem, M. İlhan, A. S. Başak and A. Mergen, *Optik*, 2016, **127**, 1918–1921.
14 M. K. Ekmekçi, M. Erdem, A. S. Başak, M. İlhan and A. Mergen, *Ceram. Int.*, 2015, **127**, 9680–9685.
15 M. G. B. Drew, R. J. Hobson and V. T. Padayatchy, *J. Mater. Chem.*, 1993, **3**, 889–892.
16 M. Sato and Y. J. Hama, *J. Solid State Chem.*, 1995, **118**, 193–198.
17 I. S. Cho, S. Lee, J. H. Noh, D. W. Kim, H. S. Jung, D. W. Kim and K. S. Hong, *Cryst. Growth Des.*, 2010, **10**, 2447–2450.
18 K. L. Keester, R. R. Neurgaonkar, T. C. Lim and E. J. Staples, *Mater. Res. Bull.*, 1980, **15**, 821–826.
19 R. G. A. Kumar, S. Hata, K. Ikeda and K. G. Gopchandran, *RSC Adv.*, 2016, **6**, 67295–67307.
20 R. Saraf, C. Shivakumara, S. Behera, H. Nagabhushana and N. Dhananjaya, *RSC Adv.*, 2015, **5**, 4109–4120.
21 K. Wahid, M. Pokhrel and Y. Mao, *J. Solid State Chem.*, 2017, **245**, 89–97.
22 B. R. Judd, *Phys. Rev.*, 1962, **127**, 750.
23 G. S. Ofelt, *J. Chem. Phys.*, 1962, **37**, 511.
24 A. Ćirić, S. Stojadinović, M. Sekulić and M. D. Dramićanin, *J. Lumin.*, 2019, **205**, 351–356.
25 M. Born and E. Wolf, *Principles of Optics*, Pergamon Press, Oxford, London, Edinburg, New York, Paris, Frankfurt, 1968.
26 S. S. Batsanov, *Structurnaya refractometria*, Visshaya Shkola, Moscow, 1976.
27 R. D. Shannon and R. X. Fischer, *Phys. Rev. B: Condens. Matter Mater. Phys.*, 2006, **73**, 235111.
28 G. B. Bokii and M. A. P. Koshits, *X-ray Structure Analysis*, MSU, Moscow, 1964.

29 A. S. Korotkov and V. V. Atuchin, *Opt. Commun.*, 2008, **281**, 2132.
30 M. İlhan and İ. Ç. Keskin, *Physica B*, 2020, **85**, 412106.
31 S. Dutta, S. Som and S. K. Sharma, *RSC Adv.*, 2018, **8**, 53–67.
32 M. H. V. Werts, R. T. F. Jukes and J. W. Verhoeven, *Phys. Chem. Chem. Phys.*, 2002, **4**, 1542–1548.
33 R. J. M. Gopinath, S. Gopi, S. M. Simon, A. C. Saritha, P. R. Biju, C. Joseph and N. V. Unnikrishnan, *RSC Adv.*, 2020, **10**, 20057–20066.